Astronomy & Astrophysics manuscript no. galmmdust
July 30, 2013

Planck intermediate results. XIV. Dust emission at millimetre wavelengths in the Galactic plane

Planck Collaboration: P. A. R. Ade[77], N. Aghanim[53], M. I. R. Alves[53*], M. Arnaud[66], M. Ashdown[63,6], F. Atrio-Barandela[18], J. Aumont[53], C. Baccigalupi[76], A. J. Banday[81,10], R. B. Barreiro[60], J. G. Bartlett[1,61], E. Battaner[83], K. Benabed[54,80], A. Benoit-Lévy[24,54,80], J.-P. Bernard[10], M. Bersanelli[32,45], P. Bielewicz[81,10,76], J. Bobin[66], A. Bonaldi[62], J. R. Bond[9], J. Borrill[13,78], F. R. Bouchet[54,80], F. Boulanger[53], M. Bucher[1], C. Burigana[44,30], R. C. Butler[44], J.-F. Cardoso[67,1,54], A. Catalano[68,65], A. Chamballu[66,15,53], H. C. Chiang[26,7], L.-Y Chiang[56], P. R. Christensen[73,35], D. L. Clements[50], S. Colombi[54,80], L. P. L. Colombo[23,61], F. Couchot[64], B. P. Crill[61,74], A. Curto[6,60], F. Cuttaia[44], L. Danese[76], R. D. Davies[62], R. J. Davis[62], P. de Bernardis[31], A. de Rosa[44], G. de Zotti[41,76], J. Delabrouille[1], C. Dickinson[62], J. M. Diego[60], H. Dole[53,52], S. Donzelli[45], O. Doré[61,11], M. Douspis[53], X. Dupac[38], T. A. Enßlin[71], H. K. Eriksen[58], E. Falgarone[65], F. Finelli[44,46], O. Forni[81,10], M. Frailis[43], E. Franceschi[44], S. Galeotta[43], K. Ganga[1], T. Ghosh[53], M. Giard[81,10], G. Giardino[39], J. González-Nuevo[60,76], K. M. Górski[61,84], A. Gregorio[33,43], A. Gruppuso[44], F. K. Hansen[58], D. Harrison[57,63], C. Hernández-Monteagudo[12,71], D. Herranz[60], S. R. Hildebrandt[11], E. Hivon[54,80], W. A. Holmes[61], A. Hornstrup[16], W. Hovest[71], A. H. Jaffe[50], W. C. Jones[26], M. Juvela[25], E. Keihänen[25], R. Keskitalo[21,13], T. S. Kisner[70], R. Kneissl[37,8], J. Knoche[71], M. Kunz[17,53,3], H. Kurki-Suonio[25,40], G. Lagache[53], A. Lähteenmäki[2,40], J.-M. Lamarre[65], A. Lasenby[6,63], R. J. Laureijs[39], C. R. Lawrence[61], R. Leonardi[38], M. Liguori[29], P. B. Lilje[58], M. Linden-Vørnle[16], M. López-Caniego[60], J. F. Macías-Pérez[68], B. Maffei[62], D. Maino[32,45], N. Mandolesi[44,5,30], M. Maris[43], D. J. Marshall[66], P. G. Martin[9], E. Martínez-González[60], S. Masi[31], S. Matarrese[29], P. Mazzotta[34], A. Melchiorri[31,47], L. Mendes[38], A. Mennella[32,45], M. Migliaccio[57,63], S. Mitra[49,61], M.-A. Miville-Deschênes[53,9], A. Moneti[54], L. Montier[81,10], G. Morgante[44], D. Mortlock[50], D. Munshi[77], J. A. Murphy[72], P. Naselsky[73,35], F. Nati[31], P. Natoli[30,4,44], H. U. Nørgaard-Nielsen[16], F. Noviello[62], D. Novikov[50], I. Novikov[73], C. A. Oxborrow[16], L. Pagano[31,47], F. Pajot[53], R. Paladini[51], D. Paoletti[44,46], F. Pasian[43], G. Patanchon[1], M. Peel[62], O. Perdereau[64], F. Perrotta[76], F. Piacentini[31], M. Piat[1], E. Pierpaoli[23], D. Pietrobon[61], S. Plaszczynski[64], E. Pointecouteau[81,10], G. Polenta[4,42], N. Ponthieu[53,48], L. Popa[55], G. W. Pratt[66], S. Prunet[54,80], J.-L. Puget[53], J. P. Rachen[20,71], W. T. Reach[82], R. Rebolo[59,14,36], M. Reinecke[71], M. Remazeilles[53,1], C. Renault[68], S. Ricciardi[44], T. Riller[71], I. Ristorcelli[81,10], G. Rocha[61,11], C. Rosset[1], J. A. Rubiño-Martín[59,36], B. Rusholme[51], M. Sandri[44], G. Savini[75], D. Scott[22], L. D. Spencer[77], J.-L. Starck[66], V. Stolyarov[6,63,79], F. Sureau[66], D. Sutton[57,63], A.-S. Suur-Uski[25,40], J.-F. Sygnet[54], J. A. Tauber[39], D. Tavagnacco[43,33], L. Terenzi[44], L. Toffolatti[19,60], M. Tomasi[45], M. Tristram[64], M. Tucci[17,64], L. Valenziano[44], J. Valiviita[40,25,58], B. Van Tent[69], P. Vielva[60], F. Villa[44], N. Vittorio[34], L. A. Wade[61], B. D. Wandelt[54,80,28], D. Yvon[15], A. Zacchei[43], and A. Zonca[27]

(Affiliations can be found after the references)

Received x July 2013/ Accepted x July 2013

ABSTRACT

We use *Planck* HFI data combined with ancillary radio data to study the emissivity index of the interstellar dust emission in the frequency range 100–353 GHz, or 3–0.8 mm, in the Galactic plane. We analyse the region $l = 20°$–$44°$ and $|b| \leq 4°$ where the free-free emission can be estimated from radio recombination line data. We fit the spectra at each sky pixel with a modified blackbody model and two spectral indices, $\beta_{\rm mm}$ and $\beta_{\rm FIR}$, below and above 353 GHz respectively. We find that $\beta_{\rm mm}$ is smaller than $\beta_{\rm FIR}$ and we detect a correlation between this low frequency power-law index and the dust optical depth at 353 GHz, τ_{353}. $\beta_{\rm mm}$ increases from about 1.53 in the more diffuse regions of the Galactic disk, $|b| = 3°$–$4°$ and $\tau_{353} \sim 5 \times 10^{-5}$, to about 1.65 in the densest regions with an optical depth of more than one order of magnitude higher. We associate this correlation with an evolution of the dust emissivity related to the fraction of molecular gas along the line of sight. This translates into $\beta_{\rm mm} \sim 1.53$ for a medium which is mostly atomic and $\beta_{\rm mm} \sim 1.65$ when the medium is dominated by molecular gas. We find that both the Two-Level System model and the emission by ferromagnetic particles can explain the results if spatial variations of the component or physical processes responsible for the flattening of the dust emission are allowed. The results improve our understanding of the physics of interstellar dust, and lead towards a complete model of the dust spectrum from far-infrared to millimetre wavelengths.

Key words. ISM: general – Galaxy: general – radiation mechanisms: general – radio continuum: ISM – submillimeter: ISM

1. Introduction

The frequency coverage of *Planck*[1] is opening new windows in our understanding of Galactic emission. This is especially the case for the high frequency data which are providing an all-sky view of the Rayleigh-Jeans regime of the thermal dust spectrum. The emission at the *Planck* high frequency bands (350 μm–3 mm) is dominated by the contribution of big grains, which heated by stellar photons are in thermal equilibrium with the interstellar radiation field (ISRF). The spectral energy distribution (SED) of big dust grains is usually approximated by a modified blackbody emission law of the form:

$$I_\nu = \tau_{\nu_0} \left(\frac{\nu}{\nu_0}\right)^\beta B_\nu(\nu, T_{\rm d}) \quad (1)$$

where τ_{ν_0} is the dust optical depth at a reference frequency ν_0, β is the spectral index of the opacity, and B_ν is the Planck func-

* Corresponding author: M. I. R. Alves, marta.alves@ias.u-psud.fr

[1] *Planck* (http://www.esa.int/Planck) is a project of the European Space Agency (ESA) with instruments provided by two scientific consortia funded by ESA member states (in particular the lead countries France and Italy), with contributions from NASA (USA) and telescope reflectors provided by a collaboration between ESA and a scientific consortium led and funded by Denmark.

tion, which depends on both the frequency and the dust temperature T_d. However, early observations by the *Cosmic Background Explorer* (*COBE*) indicated that the modified blackbody spectrum does not provide a good description of the dust SED from far-infrared (FIR) to millimetre wavelengths (Reach et al. 1995). Later works have confirmed that β appears to vary with frequency, the SED flattening in the millimetre relative to the best single modified blackbody fit, and also varying with environment (Finkbeiner et al. 1999; Galliano et al. 2005; Paladini et al. 2007; Planck Collaboration 2011c,b). Studies of dust analogues (e.g., Agladze et al. 1996; Boudet et al. 2005; Coupeaud et al. 2011) have characterized the FIR and millimetre emission of different types of amorphous silicates. These showed a frequency, as well as temperature, dependence of β not unlike the astronomical results. The astrophysical interpretation of this flattening is under study, as new observations become available, and some possible explanations have been suggested. One possibility is a description of the opacity of the big grains in terms of a Two-Level System (TLS, Paradis et al. 2012). Alternatively, it might be attributed to magnetic dipole emission from a distinct new grain component, magnetic nano-particles (Draine & Hensley 2012a).

In order to study the low-frequency flattening of the dust SED in the Galactic plane, we need to take into account free-free emission from the ionized gas. Free-free emission is a principal foreground contaminant of the Cosmic Microwave Background (CMB), not only at radio frequencies, where it is comparable to other Galactic components such as synchrotron, but also at millimetre wavelengths where the thermal dust emission dominates. It becomes a major component in the Galactic plane where it is produced by the gas ionized by recently formed massive stars. All-sky maps of the free-free emission, derived in the context of CMB foreground studies, have been obtained directly from Hα measurements (Dickinson et al. 2003; Finkbeiner 2003). However this optical line suffers from large dust absorption along the Galactic plane, and thus fails to provide a reliable measure of the thermal emission at low Galactic latitudes. A free-free map that includes the Galactic plane is essential, not only to correctly evaluate the CMB power spectrum at low angular frequency, but also for Galactic star formation studies. The *WMAP* satellite has provided all-sky maps at five microwave frequencies that have been combined to estimate the contribution of free-free, synchrotron, thermal dust and anomalous microwave emission (AME) using a maximum entropy method (MEM, Bennett et al. 2012).

Another approach using hydrogen radio recombination lines (RRLs) has been presented recently by Alves et al. (2010, 2012). In contrast to Hα these radio lines at a frequency of 1.4 GHz are optically thin and are not absorbed by dust or the radio emitting plasma. The RRL method has provided the first direct measure of the diffuse free-free emission along the Galactic plane, in the longitude range $l = 20°$–$44°$ and for latitudes $|b| \leq 4°$ (Alves et al. 2012).

Free-free emission from thermal electrons has a flat intensity spectral index given by $I \propto \nu^{\alpha}$, where

$$\alpha = -\frac{1}{10.48 + 1.5\ln(T_e/8000\,\mathrm{K}) - \ln(\nu/\mathrm{GHz})} \quad (2)$$

with T_e the electron temperature (Bennett et al. 1992; Dickinson et al. 2003). For the high-frequency range of *Planck* and the typical values of electron temperature, 7000 K, α varies between -0.18 and -0.23. Variations in the electron temperature of 2000 K do not change the free-free spectral index by more than 0.02. The free-free emission dominates at frequencies between 60 and 100 GHz, but there the other Galactic components, namely synchrotron, dust and AME, also contribute to the total intensity. The AME is an additional Galactic component observed in the frequency range 10–60 GHz (e.g., Kogut et al. 1996; Leitch et al. 1997; de Oliveira-Costa et al. 1997; Planck Collaboration 2011e, 2013a; Planck Collaboration Int. XII 2013) which cannot be explained by free-free, synchrotron or vibrational dust emission and is thought to arise from small spinning dust grains (Draine & Lazarian 1998; Ali-Haïmoud et al. 2009; Ysard & Verstraete 2010). In a spectral decomposition of the four Galactic emission components along the plane, Planck Collaboration (2013b) find that the AME contribution is comparable to that of the free-free in the frequency range 20–40 GHz. On the other hand, and due to its steeper spectral index, $-1.2 \lesssim \alpha \lesssim -1.7$ (Davies et al. 1996; Ghosh et al. 2012), the synchrotron emission is mostly dominant at frequencies less than a few gigahertz.

This paper aims to characterize for the first time the dust emissivity in the frequency range 100–353 GHz of the diffuse emission in the Galactic plane. For this purpose, we remove the free-free emission contribution using the RRL data (Sect. 3.1). We start by describing the *Planck* and ancillary data used in this work in Sects. 2 and 3. In Sect. 4 we present the data analysis techniques, followed by the main results of the paper in Sect. 5. These are further discussed and interpreted in Sect. 6, followed by the conclusions in Sect. 7.

2. *Planck* HFI data

Planck (Tauber et al. 2010; Planck Collaboration 2011a; Planck Collaboration I 2013) is the third-generation space mission to measure the anisotropy of the CMB. It observed the sky in nine frequency bands covering 28.5–857 GHz with high sensitivity and angular resolution from 32′.24 to 4′.33. The Low Frequency Instrument (LFI; Mandolesi et al. 2010; Bersanelli et al. 2010; Mennella et al. 2011; Planck Collaboration II 2013) covered the 28.4, 44.1, and 70.4 GHz bands with amplifiers cooled to 20 K. The High Frequency Instrument (HFI; Lamarre et al. 2010; Planck HFI Core Team 2011; Planck Collaboration VI 2013) covered the 100, 143, 217, 353, 545, and 857 GHz bands with bolometers cooled to 0.1 K. Polarization is measured in all but the highest two bands (Leahy et al. 2010; Rosset et al. 2010).

In the present work we use data from the *Planck* 2013 data release which can be obtained from the *Planck* Legacy Archive[2]. We use the HFI data acquired between 13 August 2009 and 27 November 2010. These are converted from units of thermodynamic temperature to intensity units (MJy sr^{-1}, Planck Collaboration IX 2013). The *Planck* CMB map, derived with the *SMICA* component separation method (Planck Collaboration XII 2013), has been inpainted in the thin disk of the Galaxy[3] to reproduce the CMB signal which cannot be correctly separated from the much brighter Galactic emission. For this reason we derive our results using the non-CMB subtracted data, which we compare with those obtained when the *SMICA* CMB map is removed from the data. The lowest HFI frequency band also has the lowest angular resolution, of 9′.65.

[2] http://www.sciops.esa.int/index.php?project=planck&page=Planck_Legacy_Archive

[3] This region is masked out and filled with a constrained realization of CMB anisotropies.

However we smooth the *Planck* data to a common resolution of 15′, assuming Gaussian beams, to match the lower resolution of the RRL data (Sect. 3.1).

The 100 GHz data are significantly contaminated by the CO J=1→0 line at 115 GHz and the 217 GHz data by the CO J=2→1 line at 230 GHz. At 353 GHz the contribution of the CO J=3→2 line is small, but not negligible compared to dust emission. The CO line emission is subtracted using the *Planck* TYPE 1 CO maps from the MILCA (Modified Independent Linear Combination Algorithm, Hurier et al. 2010) bolometer solution (Planck Collaboration XIII 2013). These are converted from line integrated units to intensity units as described in Planck Collaboration XIII (2013). The calibration uncertainties on these maps are of 10, 2, and 5 % at 100, 217, and 353 GHz, respectively. The 100 GHz MILCA map has been compared with ground-based data, in particular the Dame et al. (2001) ^{12}CO J=1→0 survey along the Galactic plane, for which there is an overall agreement of 16 % (Planck Collaboration XIII 2013). However, in the Galactic plane region of the present study, both datasets agree within 25 %. This discrepancy can be explained by the shifting of the CO line frequency due to Doppler effects, that is to say, the rotation of the Galactic disk (Planck Collaboration XIII 2013).

The overall calibration uncertainties for the *Planck* HFI maps are 10 % at 857 and 545 GHz, 1.2 % at 353 GHz, and 0.5 % at lower frequencies. These values are increased at the lowest frequencies due to the subtraction of the CO and free-free emission. We did not subtract the zodiacal light emission from the maps, because it is a negligible contribution in the Galactic plane (Planck Collaboration XIV 2013). Moreover, the cosmic infrared background (CIB) monople was removed from all the HFI maps as described in Planck Collaboration (2013c).

3. Ancillary data

Along with *Planck* HFI we need to use ancillary data, namely RRL observations for the removal of the free-free emission and *IRAS* data to constrain the dust temperature. All data sets are in `HEALPix` format (Górski et al. 2005) and are smoothed to a common resolution of 15′.

3.1. Radio Recombination Line data

A fully-sampled map of the free-free emission in the Galactic plane region $l = 20°$–$44°$ and $|b| \leq 4°$ has been derived by Alves et al. (2012) using RRL data. These data are from the H I Parkes All-Sky Survey and associated Zone of Avoidance Survey (Staveley-Smith et al. 1996, 1998) at 1.4 GHz and 15′ resolution, and have an overall calibration uncertainty of 10 %. There are possible systematic biases in the free-free estimate due to the assumed electron temperature: increasing the adopted mean value of 6000 K by 1000 K would increase the brightness temperature by 19 %. There is also a 10–20 % correction due to the conversion of antenna to brightness temperature (Alves et al. 2012). This correction is scale-dependent, thus it varies with the fraction of point source emission relative to diffuse emission.

3.2. IRAS data

We use the IRIS (Improved Reprocessing of the *IRAS* survey) data at 100 μm (Miville-Deschênes & Lagache 2005) to constrain the peak of the thermal dust emission. The calibration uncertainty for these data is 13.5 %.

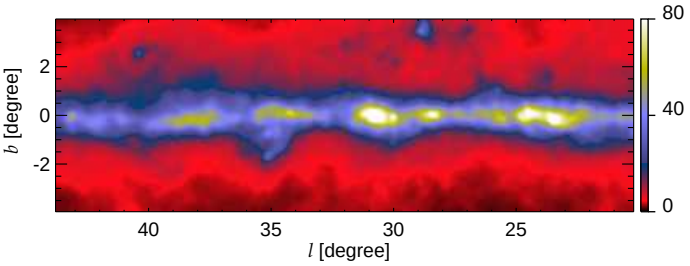

Fig. 1. HFI 353 GHz map of the Galactic plane region $l = 20°$–$44°$, $|b| \leq 4°$, in units of MJy sr^{-1} and at 15′ resolution.

4. Analysis

The aim here is to determine the power-law index of the interstellar dust opacity at the lowest HFI frequencies, which we do by fitting the dust SED.

As mentioned in Sect. 1, β appears to be frequency dependent with a break observed at frequencies around 600 GHz, or $\lambda \sim 500\,\mu$m (Paradis et al. 2009; Gordon et al. 2010; Galliano et al. 2011). Planck Collaboration (2011g) also found that a single modified blackbody curve accurately fits the FIR spectrum of Galactic molecular clouds, but leaves large residuals at frequencies below 353 GHz. For this reason we decided to fit the dust SED using a modified blackbody model, but allowing β to vary with frequency, having $\beta = \beta_{\rm FIR}$ for $\nu \geq 353$ GHz and $\beta = \beta_{\rm mm}$ for $\nu < 353$ GHz. Using the *Planck* HFI bands along with the *IRAS* 100 μm data, we also solve for the other parameters in Eq. (1), namely $T_{\rm d}$ and τ_{353}, where we take the reference frequency as 353 GHz for the dust optical depth.

The *Planck* maps at frequencies above 353 GHz contain mainly dust emission and also CIB emission. The CIB fluctuations have a power spectrum flatter than that of the interstellar dust (Miville-Deschênes et al. 2002; Lagache et al. 2007; Planck Collaboration 2011d), thus contributing mostly at small angular scales and producing a statistically homogeneous signal. This signal only represents a significant fraction of the total brightness in the most diffuse high-latitude regions of the sky, and thus can be neglected in the Galactic plane.

At frequencies below 353 GHz, even though most of the emission comes from interstellar dust, both the CMB and free-free components also contribute to the total brightness. The fluctuations of the CMB are faint, rms of about 80 μK at scales of 15′, compared to the brightest emission in the Galactic plane. Therefore, we can neglect the contribution from the CMB, since its rms temperature is about 5 % of the total emission in the thin disk of the Galaxy. However, at latitudes $|b| \gtrsim 2°$ the CMB emission at 100 GHz is about 10 times that of the free-free. The effects of neglecting the CMB component at these higher latitudes will be investigated via simulations in Sect. 5.1, as well as using the *SMICA* CMB map in Sect. 5.2.

At $|b| \lesssim 1°$, the contribution of the free-free emission can be as high as 20–40 % to the total emission at 100 GHz, from both the diffuse and the individual H II regions. Therefore, we need to remove the free-free emission if we are to fit the dust spectrum only with a modified blackbody model. For this purpose, we use the free-free map estimated from the RRLs (Sect. 3.1), as this is currently the only direct measure of this emission in the Galactic plane, in particular in the 24° × 8° region cen-

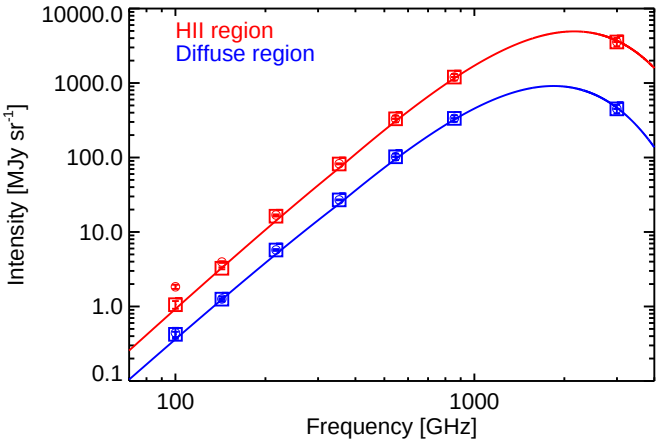

Fig. 2. Spectra towards the H II region complex W42 (red) and a diffuse region in the Galactic plane centred at (l,b) = (40.°5,0.°0) (blue). The circles show the total intensity (corrected for CO emission) and the squares show the same data after subtraction of the free-free contribution. All the data points are shown with their corresponding uncertainties.

tred on (l,b) = (32°,0°). This region is shown in Fig. 1, in the *Planck* 353 GHz channel. The RRL map is scaled from 1.4 GHz to the HFI frequencies using an average intensity spectral index of −0.2 (Sect. 1) and then subtracted from each *Planck* map. The RRL data are similarly used in the work of Planck Collaboration (2013b) to separate the different emission components in the Galactic plane, and to determine the contribution of the AME. In that work the radio data are scaled up by 10 % after comparison with two other free-free solutions given by the *Planck* `fastMEM` (Planck Collaboration 2013b) and *WMAP* MEM (Bennett et al. 2012) component separation methods, as well as for the reasons discussed in Sect. 3.1. The `fastMEM` and *WMAP* results agree within 2 % but they are about 20 % higher than the RRL solution. In this paper we adopt the same scaling for the RRL data as in Planck Collaboration (2013b); as will be discussed in the next section, this does not significantly change the main results on $\beta_{\rm mm}$.

We used the `IDL MPFIT` routine to fit the final SEDs pixel-by-pixel in the 24°×8° region. This routine performs weighted least-squares fitting of the data (Markwardt 2009), taking into account the noise (both statistical noise and systematic uncertainties) for each spectral band. We also include a noise term from the CMB fluctuations, typically 80 μK, which will be dominant outside the Galactic plane and at the lowest frequencies. These uncertainties are used to give weights to the spectral points. Colour corrections based on the local spectral index across each band were applied to both *Planck* and *IRAS* data during the model-fitting procedure (Planck Collaboration IX 2013).

5. Results from spectral fits

Fig. 2 shows the spectra at the position of a complex of H II regions, G24.5+0.0 (W42), and towards a diffuse region in the Galactic plane centred at (l,b) = (40.°5,0.°0). The fitted models are also shown. The effect of subtracting the free-free emission is clearly visible at 100 GHz in the spectrum of the H II region (compare the circles with the squares); at frequencies above 143 GHz this subtraction is negligible. The spectral indices of the H II region are $\beta_{\rm FIR} = 1.9 \pm 0.2$ and $\beta_{\rm mm} = 1.7 \pm 0.2$, while for the diffuse region, $\beta_{\rm FIR} = 1.9 \pm 0.2$ and $\beta_{\rm mm} = 1.6 \pm 0.2$. These values suggest that the diffuse region has a flatter millimetre spectrum than the H II region. The uncertainties on the parameters reflect the likely mixture of dust components along the line of sight, which have a range of temperatures and different properties. The χ^2 values of the fits are 2.7 and 1.2, for the H II region and the diffuse region respectively, with $N_{\rm dof} = 3$[4]. Similarly to the examples in Fig. 2, the reduced χ^2 values across the map are systematically lower than one, meaning that the fits are within the uncertainties of each point. The uncertainties on the data at frequencies of 217 GHz and above are dominated by the calibration uncertainties, which are correlated across the channels. At these frequencies, the median value of our fit residuals across the map is close to zero and within the overall uncertainties of the data, thus indicating that the fits are a good representation of the data. This is not the case at 100 and 143 GHz, where the histograms of the percentage residual emission are centred at 3 % and −3 %, respectively. These values are higher than the 0.5 % overall calibration uncertainty at these frequencies but lower than the final uncertainties once the noise contribution from CMB and the uncertainties associated with free-free and CO templates are included.

The distributions of temperature and spectral indices fitted for the 24° × 8° region under study are shown in Fig. 3. The dust temperature ranges from 16 to 24 K, with a median value of 19 K. Even though we are describing the SED with only a single temperature whilst a range of temperatures are expected along the line of sight especially in the Galactic plane, the higher temperature regions found here are associated with H II regions, as expected from local heating by their OB stars. Similarly, colder regions are associated with molecular clouds.

The histograms of $\beta_{\rm FIR}$ and $\beta_{\rm mm}$ are compared in Fig. 3(b) for the whole 24° × 8° region. The $\beta_{\rm FIR}$ distribution has a median value of 1.76 and a standard deviation (σ, corresponding to the 68.3 % confidence interval) of 0.08 and that of $\beta_{\rm mm}$ has a median value of 1.55 with $\sigma = 0.12$. This indicates that he $\beta_{\rm mm}$ distribution is centred at a lower value and is also broader. If we select the pixels within $|b| \lesssim 1°$, which represents regions with an optical depth $\tau_{353} \geq 4 \times 10^{-4}$, the corresponding $\beta_{\rm FIR}$ and $\beta_{\rm mm}$ histograms, shown as dashed lines, have median values of 1.88, $\sigma = 0.08$, and 1.60, $\sigma = 0.06$ respectively. The $\beta_{\rm mm}$ values fitted outside the narrow Galactic plane are affected by the CMB which becomes brighter than the free-free and is not taken into account in the fit. The impact of the CMB in the $\beta_{\rm mm}$ results will be further analysed in Sects. 5.1 and 5.2.

The histogram of $\beta_{\rm FIR}$ in Fig. 3 does not include the effects of the calibration uncertainties, namely its width only takes into account the variations across the map. This is an important point when assessing the difference between $\beta_{\rm FIR}$ and $\beta_{\rm mm}$, as given by Fig. 3. At frequencies of 353 GHz and above, where the contribution of CO, free-free and CMB are negligible compared to dust emission, the data uncertainties are dominated by calibration uncertainties. We performed Monte Carlo simulations to estimate this effect on $\beta_{\rm FIR}$ and found that, in 1000 simulations, the dispersion around an input value of 1.75 is 0.17. This value is about twice that measured from the $\beta_{\rm FIR}$ histograms of Fig. 3. Nevertheless, in the thin Galactic disk, this does not affect the difference measured between $\beta_{\rm FIR}$ and $\beta_{\rm mm}$. A further check on the quality of the SED fits and the importance of including a second spectral index, $\beta_{\rm mm}$, is given by comparing the residuals with those resulting from a model with a single β. When only one spectral index is fit for from 100 to 3000 GHz, the median

[4] Degrees of freedom (dof = $N_{\rm points} - N_{\rm parameters}$).

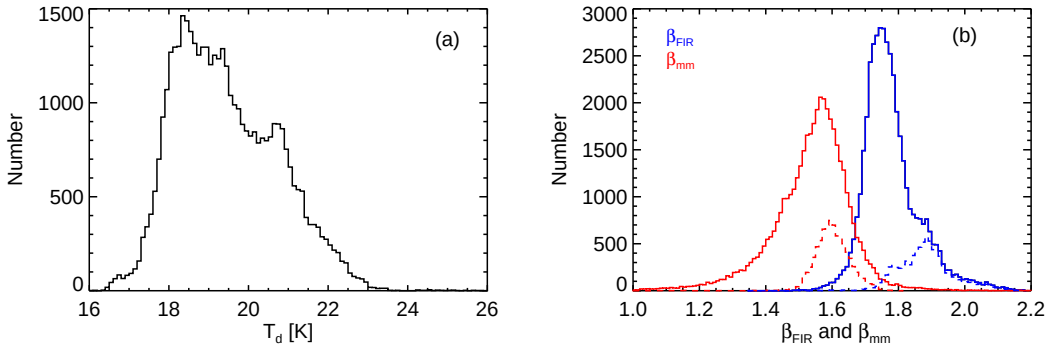

Fig. 3. Histograms of the dust temperature (a) and dust opacity indices (b) for the 24° × 8° region. The dashed lines in panel (b) correspond to the pixels where $\tau_{353} \geq 4 \times 10^{-4}$.

value of the residuals across the map is larger at all frequencies, relative to the two-β model. In particular, the median value of the residuals at 857 GHz, 11 %, is higher than the calibration uncertainty. We also note that, if we choose the reference frequency of 545 GHz, instead of 353 GHz for the break in the spectral index, the fits also result in larger residuals at all frequencies.

We tested the robustness of the fitted $\beta_{\rm mm}$ against calibration uncertainties in both the CO and the free-free templates by varying the correction of the CO and RRL contributions, at all frequencies, by 10 % (Sects. 2 and 3.1). An under-correction of either the CO or the free-free emission could in principle result in a lower $\beta_{\rm mm}$. However, as Fig. 4(a) illustrates, $\beta_{\rm mm}$ is essentially insensitive to these variations. This is due to the fact that dust is the dominant emission component at these frequencies, combined with the higher uncertainties of the data at 143 and 100 GHz.

In order to investigate the impact of the dust temperature on $\beta_{\rm mm}$, we compare the results when $T_{\rm d}$ is fixed to 19 K with those when $T_{\rm d}$ is allowed to vary in the SED fit. These are shown in Fig. 4(b), where it is seen that the distribution of $\beta_{\rm mm}$ is unaffected when using a constant or varying value of $T_{\rm d}$ across the region.

We find a correlation between $\beta_{\rm mm}$ and the optical depth τ_{353}, which is shown in Fig. 5. We note that this relates an intrinsic property of the dust, $\beta_{\rm mm}$, with an extrinsic one, τ_{353}. In Sect. 6 we will describe this empirical correlation in terms of the type of matter rather than the quantity of matter along the line of sight, given by τ_{353}. The scatter in $\beta_{\rm mm}$ at low optical depth values, or $|b| \gtrsim 1°$, is due to the CMB, as discussed above. For $\tau_{353} \geq 4 \times 10^{-4}$, $\beta_{\rm mm}$ increases in the highest optical depth regions, as foreshadowed by the results of Fig. 2, which showed an increase of $\beta_{\rm mm}$ from the diffuse to the H II region. A linear fit to the data, for $\tau_{353} \geq 4 \times 10^{-4}$, gives $\beta_{\rm mm} = (1.52 \pm 0.01) + (121 \pm 2) \times \tau_{353}$, where we have used the `IDL` routine `regress` to perform the linear regression fit, including only the errors on $\beta_{\rm mm}$. We note that the errors on τ_{353} are much lower than those on $\beta_{\rm mm}$. Moreover, the correlation coefficient[5] between these two parameters for $\tau_{353} \geq 4 \times 10^{-4}$, as given by the `MPFIT` routine, varies between 0.0 and 0.1. This indicates that it is unlikely that the correlation observed is due to the fitted model.

[5] The correlation matrix is computed from the covariance matrix; it measures the intrinsic correlation between the fit parameters.

The uncertainty on $\beta_{\rm mm}$ is statistical; including the systematic uncertainties introduced by the CMB, CO and free-free components, which are presented in Sect. 5.1, the correlation is

$$\beta_{\rm mm} = (1.52 \pm 0.02) + (120 \pm 23) \times \tau_{353}. \quad (3)$$

5.1. Simulations

In order to test the robustness of our fitting procedure against possible biases on $\beta_{\rm mm}$ associated with the separation of dust emission from CMB, free-free and CO, we apply our routine to simulated maps.

The first simulated maps include dust emission and CMB. We fix $T_{\rm d}$ to 19 K, $\beta_{\rm FIR}$ to 1.75 and $\beta_{\rm mm}$ to 1.52 across the region. The distribution of τ_{353} is that obtained from the fit to the data. We reproduce the dust maps at each frequency with a modified blackbody law and add them to the CMB map, reproduced from the best-fit ΛCDM model. We then apply the SED fitting routine and recover $\beta_{\rm mm}$ as a function of the input optical depth as shown in Fig. 6(a). A linear fit to the points with $\tau_{353} \geq 4 \times 10^{-4}$ gives $\beta_{\rm mm} = 1.53 - 8 \times \tau_{353}$. As discussed in Sect. 5, the scatter on the $\beta_{\rm mm}$ values for $\tau_{353} \lesssim 4 \times 10^{-4}$ is created by the CMB when this component is not taken into account in the fit. Moreover, even though it is a minor contributor in the Galactic disk, the CMB also affects the results for higher values of τ_{353}, broadening the $\beta_{\rm mm}$ distribution around the input value of 1.52 by 0.01. Thus this result shows that if there is no intrinsic correlation between these two parameters only a limited correlation will be detected. More importantly, Fig. 6(a) shows that the CMB is not responsible for the $\beta_{\rm mm}$–τ_{353} correlation derived in the previous section.

We also tested our results for a possible bias introduced by incorrect subtraction of CO and free-free emission from simulated dust maps produced as described above. For that we use the MILCA CO maps (Sect. 2) and subtract 10 % of their emission at 100, 217, and 353 GHz. Similarly we remove 10 % of the RRL free-free emission from the simulated dust maps at all frequencies. Such a correction steepens the dust spectrum, as we can see from the results of Fig. 6(b). A linear fit to the points gives $\beta_{\rm mm} = 1.53 + 22 \times \tau_{353}$. This is not, however, capable of reproducing the much steeper slope of $\beta_{\rm mm}$ with the dust optical depth. For that to be the case, both the CO and RRL maps would have to be systematically underestimated by 30 %.

We thus conclude that neither the uncertainty in the CO and free-free correction of the maps nor omitting the CMB in the spectral fits is responsible for the correlation of $\beta_{\rm mm}$ with τ_{353}. Finally, Fig. 7 shows the map of $\beta_{\rm mm}$, estimated using Eq. (3), which presents the same structure as the map of τ_{353}. On the

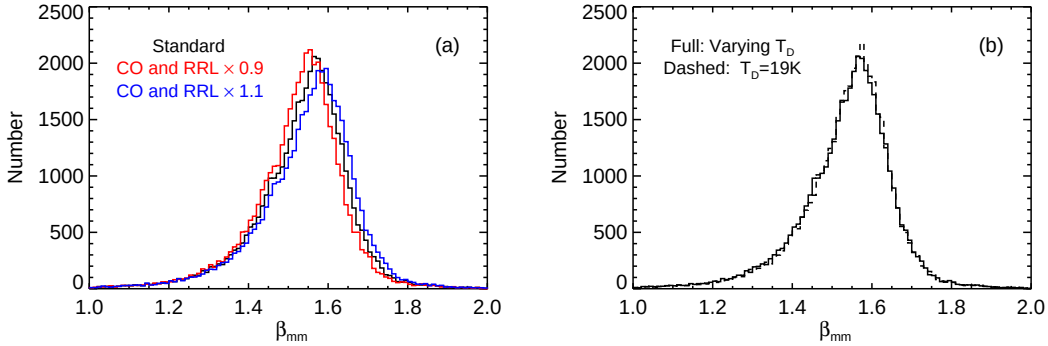

Fig. 4. Comparison of the results on $\beta_{\rm mm}$. (a) When the CO and free-free corrections vary by 10 %. (b) When $T_{\rm d}$ is allowed to vary in the fit and also when $T_{\rm d}$ is fixed to a single value of 19 K.

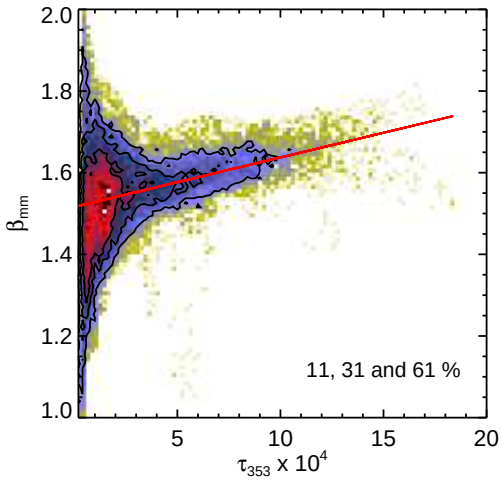

Fig. 5. $\beta_{\rm mm}$ as a function of τ_{353}, for the whole region. The red line gives the best linear fit for $\tau_{353} \geq 4 \times 10^{-4}$ (see text). The colour scale is logarithmic and it represents the density of points. The three contours show the densities for a cumulated fraction of 11, 31, and 61 % of the data points, from red to yellow.

other hand, there is no apparent correlation between the maps of $\beta_{\rm mm}$ and $T_{\rm d}$, as it will be discussed in Sect. 6.

5.2. Using the Planck SMICA CMB map

In this section we compare our results with those obtained when the *SMICA* CMB map is subtracted from each channel map before fitting the dust spectra with a modified blackbody. The resulting $\beta_{\rm mm}$ as a function of τ_{353} is shown in Fig. 8. As expected, the scatter on $\beta_{\rm mm}$ at low values of τ_{353} decreases, due to the subtraction of the CMB from the total emission, showing a tighter correlation between $\beta_{\rm mm}$ and τ_{353} at all values of optical depth. A linear fit to the data gives $\beta_{\rm mm} = (1.52 \pm 0.01) + (114 \pm 1) \times \tau_{353}$. This result confirms that the CMB is indeed a small contribution in the Galactic disk, here measured with the *SMICA* solution, and that it does not affect the main results of the work.

6. Towards a physical interpretation of the millimetre dust emissivity

In this section we compare our results with predictions from current dust models and interpret the empirical relation found between $\beta_{\rm mm}$ and τ_{353}.

An anti-correlation between β and $T_{\rm d}$ has been detected in previous observations in a variety of Galactic regions (Dupac et al. 2003; Désert et al. 2008; Paradis et al. 2010; Planck Collaboration 2011g). This seems to indicate that the dust opacity index decreases with temperature, even if part of this effect can be attributed to data noise, to the intrinsic correlation introduced in the analysis methods, and to temperature mixing along the line of sight (Sajina et al. 2006; Shetty et al. 2009b,a; Juvela & Ysard 2012b,a). Fig. 9(a) shows $\beta_{\rm FIR}$ as a function of $T_{\rm d}$, for all the points in the $24^\circ \times 8^\circ$ region. The correlation coefficient between these two parameters, from the `MPFIT` routine, is around -0.95 across the map. This implies that the fitted model is creating an anti-correlation between $\beta_{\rm FIR}$ and $T_{\rm d}$. However, such a strong anti-correlation is not observed in Fig. 9(a), nor in Fig. 9(b), where $\beta_{\rm FIR} - T_{\rm d}$ is plotted for the thin Galactic disk, $|b| \lesssim 1^\circ$. Therefore, there is a real variation of $\beta_{\rm FIR}$ across this region which decreases the anti-correlation trend generated by the model.

Fig. 9(c) shows $\beta_{\rm mm}$ as a function of $T_{\rm d}$, for the thin Galactic disk, where $\tau_{353} \geq 4 \times 10^{-4}$. For this region, the correlation coefficient between $\beta_{\rm mm}$ and $T_{\rm d}$ varies between -0.05 and -0.02, meaning that there is no significant correlation between these two parameters. The expected intrinsic anti-correlation between $\beta_{\rm mm}$ and $T_{\rm d}$ is detected outside the Galactic disk, where the signal-to-noise ratio decreases due to the CMB noise term included in the data uncertainties. Thus, Fig. 9(c) indicates that there is no evident trend of $\beta_{\rm mm}$ with $T_{\rm d}$, as it is also seen by comparing the corresponding maps in Fig. 9. We note the reader that the range of temperatures that we are probing is limited, about 6 K, which may be due to temperature mixing along the line of sight and local temperature increases around the heating sources present in the Galactic plane.

6.1. Dust models

6.1.1. Silicate-carbon models

We start by comparing our results with the predictions of two commonly used dust models, DL07 (Draine & Li 2007) and DustEM (Compiègne et al. 2011). In particular, we want to investigate whether such models, with two populations of grains

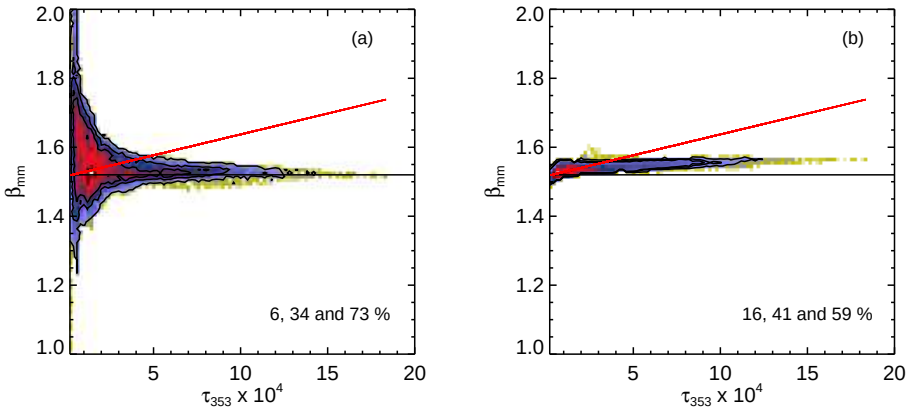

Fig. 6. β_{mm} recovered from the simulated maps, as a function of the input τ_{353}. The simulated maps in (a) have dust emission and CMB, and in (b) consist of dust, free-free and CO emission. The black line shows the input β_{mm} of 1.52 in each case; the red lines give the β_{mm}–τ_{353} relationship derived in Sect. 5. The colour scale is logarithmic and it represents the density of points. The three contours show the densities for the cumulated fractions, given by the values in each panel, of the data points, from red to yellow.

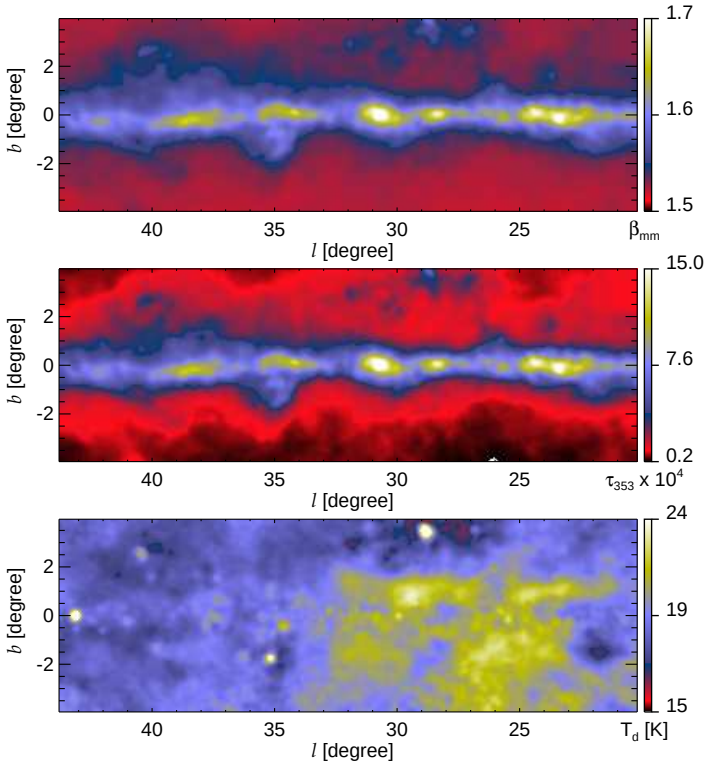

Fig. 7. Maps of β_{mm} (top), which results from the best linear fit to the correlation with optical depth given by Eq. (3), τ_{353} (middle) and T_d (bottom).

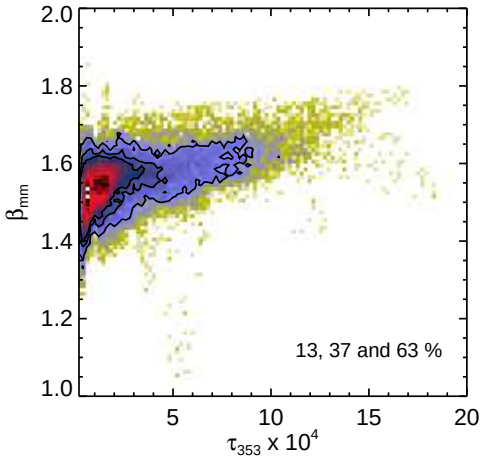

Fig. 8. β_{mm} as a function of τ_{353}, for the whole region, when the *SMICA* CMB map is subtracted from each channel map. The red line gives the best linear fit. The colour scale is logarithmic and it represents the density of points. The three contours show the densities for a cumulated fraction of 13, 37, and 63 % of the data points, from red to yellow.

dominating the emission at long wavelengths, can explain the flattening of the dust spectrum detected in the present work. Both models use the same optical properties for silicates, for which the opacity scales as $\nu^{1.6}$, for $\lambda \gtrsim 250\,\mu$m or $\nu \lesssim 1200$ GHz. For the carbon grains DL07 uses the optical properties of graphite, with a spectral index of 2, whereas DustEM uses the laboratory measurements of amorphous carbon, for which the spectral index is 1.6. We use both models to predict the emission in the photometric bands considered in this work, namely *IRAS* 100 μm and HFI, taking the standard size distribution for the diffuse Galactic emission. In order to reproduce conditions closer to those in the Galactic plane, we generate the SEDs for G_0 values of 1, 2 and 4, where G_0 is the scaling applied to the standard ISRF of Mathis et al. (1983). We then fit the spectra in the same way as the data, namely with a modified blackbody law and two spectral indices, β_{FIR} and β_{mm}. The results are shown in Table 1. First we note that when the radiation field is higher, the peak of the SED is moved to higher frequencies, where the opacity spectral index of silicate grains is larger than 1.6. This can explain the slight increase in β_{FIR} with G_0. The results also show that β_{mm} is lower than β_{FIR}, for both models. Moreover, β_{mm} does not seem to vary with G_0 or with T_d. We find that such models, including two dust components with different opacities can in principle explain the flattening of the dust emission, even if the β values recovered from their spectra are lower than those measured from the data.

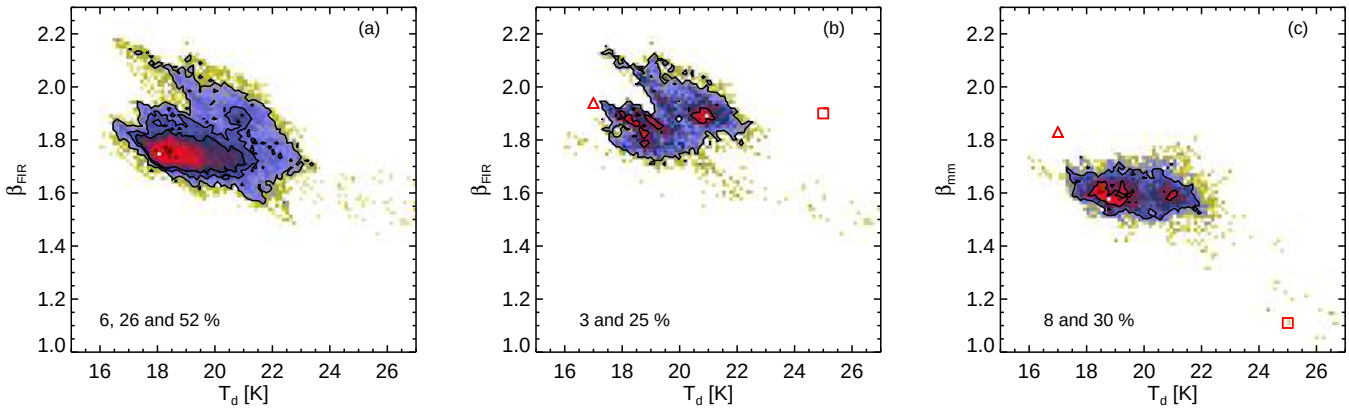

Fig. 9. Dust spectral indices as a function of temperature. (a) $\beta_{\rm FIR}$ versus $T_{\rm d}$ for the whole $24^\circ \times 8^\circ$ region. (b) $\beta_{\rm FIR}$ versus $T_{\rm d}$ for points where $\tau_{353} \geq 4 \times 10^{-4}$. (c) $\beta_{\rm mm}$ versus $T_{\rm d}$ for points where $\tau_{353} \geq 4 \times 10^{-4}$. The triangle and square in panels (b) and (c) indicate the values obtained by fitting the emissivities predicted by the TLS model (Paradis et al. 2011) for $T_{\rm d} = 17$ and 25 K (see text). The colour scale is logarithmic and it represents the density of points. The contours show the densities for the cumulated fractions, given by the values in each panel, of the data points, from red to yellow.

Table 1. Results from a modified blackbody fit to the DL07 and DustEM spectra for different scalings of the ISRF, given by G_0.

	DL07			DustEM		
G_0	$T_{\rm d}$ [K]	$\beta_{\rm FIR}$	$\beta_{\rm mm}$	$T_{\rm d}$ [K]	$\beta_{\rm FIR}$	$\beta_{\rm mm}$
1	21.8	1.65	1.43	20.1	1.58	1.48
2	24.1	1.70	1.43	22.4	1.62	1.47
4	26.7	1.73	1.43	25.0	1.64	1.46

6.1.2. Two-Level System

The Two-level System (TLS, Meny et al. 2007) model has been proposed to explain the flattening of the dust emission and its evolution with temperature. This model consists of three mechanisms which describe the interaction of electromagnetic waves with an amorphous solid. These are temperature-dependent and important in the sub-millimetre, for the range of temperatures relevant to this work. Paradis et al. (2011) use the TLS model to fit the spectrum of the diffuse Galactic emission as well as the spectra of the Archeops sources (Désert et al. 2008). Within this model, the opacity spectral index decreases with increasing temperature. We compare the emissivities predicted by TLS and given in Paradis et al. (2011) with our results for the relevant photometric bands. In particular, we select two spectra, with $T_{\rm d}$ of 17 and 25 K, within the range of temperatures probed in the present work. We apply our fitting routine to the TLS SEDs to recover $\beta_{\rm FIR}$ and $\beta_{\rm mm}$, which are shown in Figs. 9(b) and (c). The resulting $\beta_{\rm FIR}$ values are within the range found in this work, showing a small variation with temperature. However, that is not the case for $\beta_{\rm mm}$. The values predicted by the TLS model are not within the range of values found in the Galactic disk, and show a steep dependence with temperature. We note that the TLS emissivities used here were computed for a given set of parameters, derived from the best fit to the diffuse Galactic emission spectrum. Moreover, they are derived for a single grain, rather than for a grain size distribution. We could argue that the dust temperature estimated from the modified blackbody fit used here is not comparable with that derived from the TLS model. However Paradis et al. (2012) show that both temperatures agree up to about 25 K. Still, we note that $T_{\rm d}$ obtained from their modified blackbody fit assumes $\beta_{\rm FIR} = 2$. We conclude that the TLS model predicts variations of $\beta_{\rm mm}$ which are not apparent in the data. We note, however, that the range of temperatures sampled by the data is limited and that, if spatial variations of the TLS amplitude related to the degree of dust amorphization were allowed, they could easily hide the temperature dependence of $\beta_{\rm mm}$ in the data.

6.1.3. Magnetic Dipole Emission

Draine & Hensley (2012b) have proposed a dust model in which metallic nanoparticles can explain the excess emission at millimetre wavelengths, such as that observed in the Small Magellanic Cloud (SMC) (Planck Collaboration 2011c; Draine & Hensley 2012c). According to their model the iron missing from the gas phase can be locked up in solid grains, either as inclusions in larger grains, in which case they are at the same temperature as the diffuse interstellar medium (ISM), $T_{\rm d} \approx 18$ K, or as free-flying nanoparticles, which then have a higher temperature, $T_{\rm d} \approx 40$ K. The emission by these particles above their resonance frequency, $\nu \sim 15$ GHz, and below 353 GHz, is that of a blackbody. In order to test this model, we fit the dust SEDs in the region under study with a modified blackbody of a single opacity index $\beta_{\rm FIR}$. Its value is determined using the *IRAS* and HFI 857, 545, and 353 GHz points and then used to extrapolate the emission to lower frequencies. We include a blackbody spectrum, at the same temperature $T_{\rm d}$, to represent the metallic particles as inclusions in larger grains, which will account for the excess emission. We find that, at 100 GHz, the ratio between the emission from the iron dust particles and that from the modified blackbody has a median of 27 % across the $24^\circ \times 8^\circ$ region. Fig. 10 shows the results for the same H II and diffuse regions as in Fig. 2, for which this ratio is 35 % and 47 %, respectively. The contribution by the metallic particles is higher for the diffuse region since its SED is flatter at lower frequencies than that of the H II region (Sect. 5). Draine & Hensley (2012b) show that 100 % of the iron is allowed to be in the form of nanoparticles without exceeding the observed diffuse Galactic emission; their contribution relative to that of the DL07 model, at 100 GHz, is of the same order as the value found here. Therefore, we conclude that our results are within the range of plausible models,

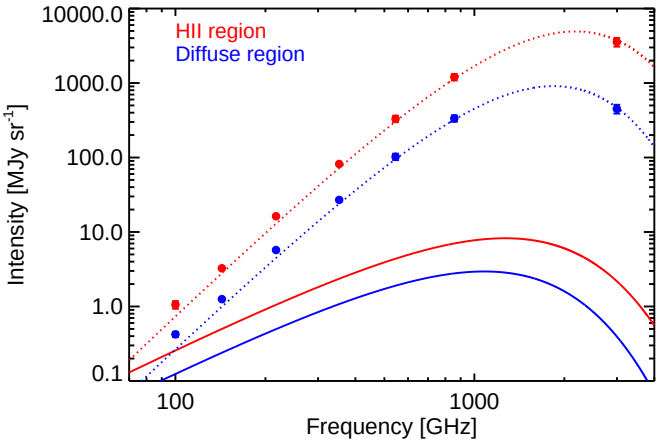

Fig. 10. Spectra towards the H II region complex W42 (red) and a diffuse region in the Galactic plane centred at $(l,b) = (40.^{\circ}5, 0.^{\circ}0)$ (blue). The circles show the total intensity, with their corresponding uncertainties. The dotted lines represent the modified blackbody model, where one single opacity spectral index is fitted to *IRAS* 100 μm and HFI 857, 545, and 353 GHz data. The solid lines represent the emission from the metallic dust particles (Draine & Hensley 2012b), at the same temperature $T_{\rm d}$. The contribution by iron particles to the total emission at 100 GHz is 35 % and 47 % for the H II and diffuse regions, respectively.

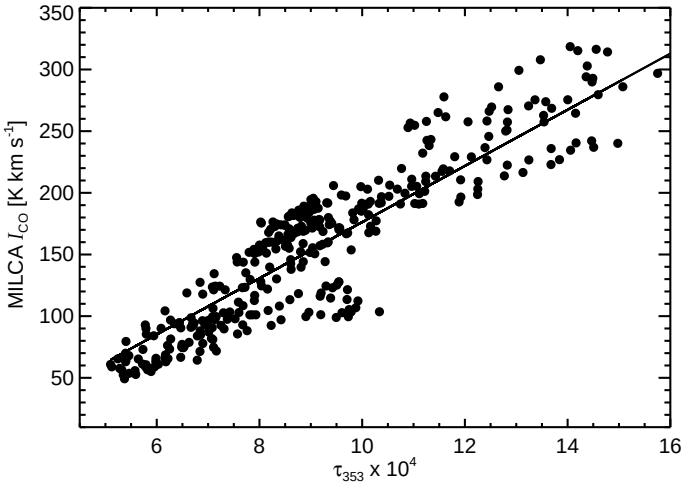

Fig. 11. The MILCA CO line intensity as a function of the dust optical depth τ_{353}, along $b = 0^{\circ}$ in the $l = 20^{\circ}$–44° region. The line represents the linear fit to the points, from which the conversion factor $X_{\rm CO} = 1.7 \times 10^{20}\,{\rm cm^{-2}\,(K\,km\,s^{-1})^{-1}}$ is derived (see text).

although suggesting a fraction of cosmic iron in magnetic particles lower than 100 %.

6.2. Correlation between $\beta_{\rm mm}$ and τ_{353}

In this section we attempt to provide a phenomenological interpretation of the empirical correlation detected between $\beta_{\rm mm}$ and τ_{353}. As mentioned in Sect. 5, the dust optical depth provides a measure of the quantity of matter along the line of sight, which may be atomic or molecular and which has the contribution of both dense clumps and diffuse media. We suggest that this variation of $\beta_{\rm mm}$ with the dust optical depth can be translated into an evolution with the fraction of molecular gas along the line of sight.

The fraction of molecular gas is given by $f_{\rm H_2} = 2N_{\rm H_2}/N_{\rm H}^{\rm tot}$. The column density of molecular hydrogen can be estimated by using the conversion factor $X_{\rm CO} = N_{\rm H_2}/I_{\rm CO}$, where $I_{\rm CO}$ is the ^{12}CO J=1→0 integrated line intensity. The Galactic $X_{\rm CO}$ conversion factor has been estimated in a variety of ways, including the use of optically thin tracers of column density such as dust emission, molecular and atomic lines, as well as using γ-ray emission. Bolatto et al. (2013) give $X_{\rm CO} = 2.0 \times 10^{20}\,{\rm cm^{-2}\,(K\,km\,s^{-1})^{-1}}$, with 30 % uncertainty, as the recommended value to use in Galactic studies. We can obtain an estimate of $X_{\rm CO}$ with the present data using the dust optical depth and the CO emission provided by the MILCA map. For that we need to include the opacity per unit gas column density of the molecular gas. Dust properties are known to evolve from the diffuse ISM to the higher density environment of molecular clouds due to grain coagulation, giving rise to an enhancement of the dust emissivity (Stepnik et al. 2003; Köhler et al. 2012). It is a factor of 2–4 times higher than the average value in the high Galactic latitude diffuse atomic ISM (Planck Collaboration 2011f,g; Martin et al. 2012). In the present work we assume that the opacity in the molecular medium is twice that in the atomic gas. Hence, the conversion factor can be written as

$$X_{\rm CO} = \frac{\tau_{353}}{I_{\rm CO}} \frac{1}{4} \frac{N_{\rm H\,I}}{\tau_{353}} \qquad (4)$$

where $\tau_{353}/N_{\rm H\,I} = 8 \times 10^{-27}\,{\rm cm^2\,H^{-1}}$ (Planck Collaboration 2013c).

Fig. 11 shows the correlation between CO intensity and dust optical depth. The points correspond to the data along $b = 0^{\circ}$ in the $l = 20^{\circ}$–44° region, where we assume that the variations in the opacity along the line of sight are dominated by molecular gas. A linear fit to the data, combined with Eq. (4), gives $X_{\rm CO} = 1.4 \times 10^{20}\,{\rm cm^{-2}\,(K\,km\,s^{-1})^{-1}}$. The uncertainty on this value is of 16 %, estimated from the scatter of the points. The fit has an offset of $\tau_{353} \sim 2.3 \times 10^{-4}$ for $I_{\rm CO} = 0\,{\rm K\,km\,s^{-1}}$, which could be attributed to the mean contribution by the atomic medium. We note that the MILCA CO data in this region of the Galactic plane are about 25 % higher than the CO data from Dame et al. (2001) (Sect. 2). Since the $X_{\rm CO}$ values in the literature refer to the Dame et al. data, we scale our result by 25 % which gives $X_{\rm CO} = 1.7 \times 10^{20}\,{\rm cm^{-2}\,(K\,km\,s^{-1})^{-1}}$. Therefore, the value found here using our conversion from τ_{353} to $N_{\rm H_2}$, is consistent with the recommended value for the Galaxy given by Bolatto et al. (2013).

With an estimate of $X_{\rm CO}$ for the region under study, along with the assumption that the dust opacity in the molecular gas is twice that in the atomic gas, we are able to derive $f_{\rm H_2}$. Fig. 12 shows that $\beta_{\rm mm}$ increases with $f_{\rm H_2}$, showing an evolution of the millimetre dust emission from atomic to molecular dominated regions. A linear fit to the data gives $\beta_{\rm mm} = (1.53 \pm 0.01) + (0.12 \pm 0.01)\,f_{\rm H_2}$, meaning that $\beta_{\rm mm} = 1.53$ and 1.65 at low and high values of $f_{\rm H_2}$, respectively. We note that we have assumed a single $T_{\rm d}$ value in the SED fit, ignoring the fact that $T_{\rm d}$ is likely to be systematically lower in molecular clouds than in the diffuse atomic medium (Planck Collaboration 2011b). However, since $T_{\rm d}$ and $\beta_{\rm mm}$ are anti-correlated, using a lower $T_{\rm d}$ in the fit would result in an even higher $\beta_{\rm mm}$ in molecular media. This would thus increase the difference in $\beta_{\rm mm}$ between atomic and molecular dominated regions.

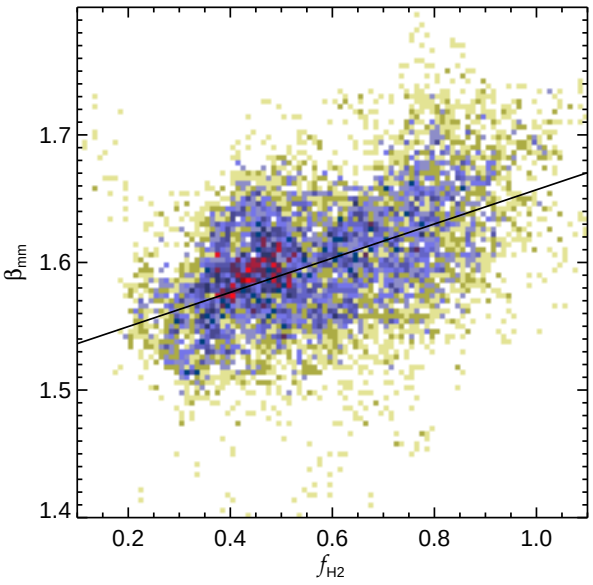

Fig. 12. β_{mm} as a function of f_{H_2}, the fraction of molecular gas along the line of sight. Note that the points correspond to the thin Galactic disk, $|b| \lesssim 1^\circ$ or $\tau_{353} \geq 4 \times 10^{-4}$. Here f_{H_2} is estimated assuming that the dust opacity in the molecular phase is twice as that of the atomic medium and using $X_{CO} = 1.7 \times 10^{20}\,\mathrm{cm^{-2}\,(K\,km\,s^{-1})^{-1}}$. The distribution of points is relatively even across the x and y axes.

If we assume that the opacity in the molecular medium is 1.5 times higher than that in the atomic gas, instead of two times higher, then we derive an X_{CO} value of $1.8 \times 10^{20}\,\mathrm{cm^{-2}\,(K\,km\,s^{-1})^{-1}}$ or $2.3 \times 10^{20}\,\mathrm{cm^{-2}\,(K\,km\,s^{-1})^{-1}}$ with relation to the Dame et al. (2001) CO survey. Despite the 30 % difference, this result is still within the range of typical values for the Galaxy (Bolatto et al. 2013). More importantly, the correlation between β_{mm} and f_{H_2} is essentially unchanged, with a best linear fit given by $\beta_{mm} = (1.52 \pm 0.01) + (0.13 \pm 0.01)\, f_{H_2}$.

Finally we note that the evolution of β_{mm} found here could be related to the change in dust opacity observed from diffuse to molecular media (Stepnik et al. 2003). Coagulation models indicate that dust aggregation produces an overall increase of the opacity but does not significantly change the apparent β_{mm} (Köhler et al. 2012). Therefore, the correlation with the molecular material observed here remains phenomenological and its origin does not rely on a physical model.

7. Conclusions

We have used *Planck* HFI data to derive the power-law index of the interstellar dust opacity in the frequency range 100 to 353 GHz, in a $24^\circ(l) \times 8^\circ(b)$ region of the Galactic plane. This is possible to achieve after the removal of the free-free emission contribution at these frequencies, which can be as high as 20–40 % of the total emission in the thin and ionized disk of the Galaxy. Here we summarize our results:

– The spectral index of the dust opacity in the millimetre wavelength range, β_{mm}, and in the Galactic plane has a median value of 1.60 ± 0.06. Thus β_{mm} is smaller than that at FIR frequencies, β_{FIR}, for which we determine a median value of 1.88 ± 0.08.
– We find that there is no apparent trend of β_{mm} with temperature, as opposed to β_{FIR}, for which the anti-correlation has been examined in several previous studies.
– We find that β_{mm} is, however, correlated with the derived dust optical depth at 353 GHz. We interpret this correlation as an evolution of β_{mm} with the fraction of molecular gas along the line of sight, f_{H_2}. Within this scenario, $\beta_{mm} \sim 1.53$ when the medium is mostly atomic, whereas it increases to about 1.65 when the medium is predominantly molecular.
– The results on β_{mm} are compared with predictions from two different physical models, TLS and emission by ferromagnetic grains, which have been suggested to explain the flattening of the dust emission observed at long wavelengths. We find that both models can in principle explain the results. The same applies to the standard, two dust component models, such as DL07 and DustEM.

These results are important for understanding the dust emission from FIR to millimetre wavelengths. They are key for Galactic component separation, in particular for determining the spectral shape of the AME at high frequencies. Knowledge of the dust spectrum is also critical for estimates of the free-free emission from microwave CMB data.

Acknowledgements. We acknowledge the use of the `HEALPix` (Górski et al. 2005) package and *IRAS* data. The Planck Collaboration acknowledges the support of: ESA; CNES and CNRS/INSU-IN2P3-INP (France); ASI, CNR, and INAF (Italy); NASA and DoE (USA); STFC and UKSA (UK); CSIC, MICINN and JA (Spain); Tekes, AoF and CSC (Finland); DLR and MPG (Germany); CSA (Canada); DTU Space (Denmark); SER/SSO (Switzerland); RCN (Norway); SFI (Ireland); FCT/MCTES (Portugal); and DEISA (EU). A detailed description of the Planck Collaboration and a list of its members can be found at `http://www.rssd.esa.int/index.php?project=PLANCK&page=Planck_Collaboration`.

References

Agladze, N. I., Sievers, A. J., Jones, S. A., Burlitch, J. M., & Beckwith, S. V. W. 1996, ApJ, 462, 1026
Ali-Haïmoud, Y., Hirata, C. M., & Dickinson, C. 2009, MNRAS, 395, 1055
Alves, M. I. R., Davies, R. D., Dickinson, C., et al. 2012, MNRAS, 422, 2429
Alves, M. I. R., Davies, R. D., Dickinson, C., et al. 2010, MNRAS, 405, 1654
Bennett, C. L., Larson, D., Weiland, J. L., et al. 2012, ArXiv e-prints, 1212.5225
Bennett, C. L., Smoot, G. F., Hinshaw, G., et al. 1992, ApJ, 396, L7
Bersanelli, M., Mandolesi, N., Butler, R. C., et al. 2010, A&A, 520, A4
Bolatto, A. D., Wolfire, M., & Leroy, A. K. 2013, ArXiv e-prints, 1301.3498
Boudet, N., Mutschke, H., Nayral, C., et al. 2005, ApJ, 633, 272
Compiègne, M., Verstraete, L., Jones, A., et al. 2011, A&A, 525, A103
Coupeaud, A., Demyk, K., Meny, C., et al. 2011, A&A, 535, A124
Dame, T. M., Hartmann, D., & Thaddeus, P. 2001, ApJ, 547, 792
Davies, R. D., Watson, R. A., & Gutierrez, C. M. 1996, MNRAS, 278, 925
de Oliveira-Costa, A., Kogut, A., Devlin, M. J., et al. 1997, ApJ, 482, L17
Désert, F.-X., Macías-Pérez, J. F., Mayet, F., et al. 2008, A&A, 481, 411
Dickinson, C., Davies, R. D., & Davis, R. J. 2003, MNRAS, 341, 369
Draine, B. T. & Hensley, B. 2012a, ArXiv e-prints, 1205.7021
Draine, B. T. & Hensley, B. 2012b, ArXiv e-prints, 1205.7021
Draine, B. T. & Hensley, B. 2012c, ApJ, 757, 103
Draine, B. T. & Lazarian, A. 1998, ApJ, 494, L19
Draine, B. T. & Li, A. 2007, ApJ, 657, 810
Dupac, X., Bernard, J.-P., Boudet, N., et al. 2003, A&A, 404, L11
Finkbeiner, D. P. 2003, ApJS, 146, 407
Finkbeiner, D. P., Davis, M., & Schlegel, D. J. 1999, ApJ, 524, 867
Galliano, F., Hony, S., Bernard, J.-P., et al. 2011, A&A, 536, A88
Galliano, F., Madden, S. C., Jones, A. P., Wilson, C. D., & Bernard, J.-P. 2005, A&A, 434, 867
Ghosh, T., Banday, A. J., Jaffe, T., et al. 2012, MNRAS, 422, 3617
Gordon, K. D., Galliano, F., Hony, S., et al. 2010, A&A, 518, L89
Górski, K. M., Hivon, E., Banday, A. J., et al. 2005, ApJ, 622, 759
Hurier, G., Hildebrandt, S. R., & Macias-Perez, J. F. 2010, ArXiv e-prints, 1007.1149
Juvela, M. & Ysard, N. 2012a, A&A, 541, A33
Juvela, M. & Ysard, N. 2012b, A&A, 539, A71
Kogut, A., Banday, A. J., Bennett, C. L., et al. 1996, ApJ, 464, L5

Köhler, M., Stepnik, B., Jones, A. P., et al. 2012, A&A, 548, A61
Lagache, G., Bavouzet, N., Fernandez-Conde, N., et al. 2007, ApJ, 665, L89
Lamarre, J., Puget, J., Ade, P. A. R., et al. 2010, A&A, 520, A9
Leahy, J. P., Bersanelli, M., D'Arcangelo, O., et al. 2010, A&A, 520, A8
Leitch, E. M., Readhead, A. C. S., Pearson, T. J., & Myers, S. T. 1997, ApJ, 486, L23
Mandolesi, N., Bersanelli, M., Butler, R. C., et al. 2010, A&A, 520, A3
Markwardt, C. B. 2009, in Astronomical Society of the Pacific Conference Series, Vol. 411, Astronomical Data Analysis Software and Systems XVIII, ed. D. A. Bohlender, D. Durand, & P. Dowler, 251
Martin, P. G., Roy, A., Bontemps, S., et al. 2012, ApJ, 751, 28
Mathis, J. S., Mezger, P. G., & Panagia, N. 1983, A&A, 128, 212
Mennella et al. 2011, A&A, 536, A3
Meny, C., Gromov, V., Boudet, N., et al. 2007, A&A, 468, 171
Miville-Deschênes, M. & Lagache, G. 2005, ApJS, 157, 302
Miville-Deschênes, M.-A., Lagache, G., & Puget, J.-L. 2002, A&A, 393, 749
Paladini, R., Montier, L., Giard, M., et al. 2007, A&A, 465, 839
Paradis, D., Bernard, J.-P., & Mény, C. 2009, A&A, 506, 745
Paradis, D., Bernard, J.-P., Mény, C., & Gromov, V. 2011, A&A, 534, A118
Paradis, D., Paladini, R., Noriega-Crespo, A., et al. 2012, A&A, 537, A113
Paradis, D., Veneziani, M., Noriega-Crespo, A., et al. 2010, A&A, 520, L8
Planck Collaboration. 2011a, A&A, 536, A1
Planck Collaboration. 2011b, A&A, 536, A19
Planck Collaboration. 2011c, A&A, 536, A17
Planck Collaboration. 2011d, A&A, 536, A18
Planck Collaboration. 2011e, A&A, 536, A20
Planck Collaboration. 2011f, A&A, 536, A24
Planck Collaboration. 2011g, A&A, 536, A25
Planck Collaboration. 2013a, In preparation, PIP80
Planck Collaboration. 2013b, In preparation, PIP79
Planck Collaboration. 2013c, In preparation, CPP06b
Planck Collaboration I. 2013, ArXiv e-prints, 1303.5062
Planck Collaboration II. 2013, ArXiv e-prints, 1303.5063
Planck Collaboration Int. XII. 2013, ArXiv e-prints, 1301.5839
Planck Collaboration IX. 2013, ArXiv e-prints, 1303.5070
Planck Collaboration VI. 2013, ArXiv e-prints, 1303.5067
Planck Collaboration XII. 2013, ArXiv e-prints, 1303.5072
Planck Collaboration XIII. 2013, ArXiv e-prints, 1303.5073
Planck Collaboration XIV. 2013, ArXiv e-prints, 1303.5074
Planck HFI Core Team. 2011, A&A, 536, A4
Reach, W. T., Dwek, E., Fixsen, D. J., et al. 1995, ApJ, 451, 188
Rosset, C., Tristram, M., Ponthieu, N., et al. 2010, A&A, 520, A13
Sajina, A., Scott, D., Dennefeld, M., et al. 2006, MNRAS, 369, 939
Shetty, R., Kauffmann, J., Schnee, S., & Goodman, A. A. 2009a, ApJ, 696, 676
Shetty, R., Kauffmann, J., Schnee, S., Goodman, A. A., & Ercolano, B. 2009b, ApJ, 696, 2234
Staveley-Smith, L., Juraszek, S., Koribalski, B. S., et al. 1998, AJ, 116, 2717
Staveley-Smith, L., Wilson, W. E., Bird, T. S., et al. 1996, Publications of the Astronomical Society of Australia, 13, 243
Stepnik, B., Abergel, A., Bernard, J.-P., et al. 2003, A&A, 398, 551
Tauber, J. A., Mandolesi, N., Puget, J., et al. 2010, A&A, 520, A1
Ysard, N. & Verstraete, L. 2010, A&A, 509, A12

[1] APC, AstroParticule et Cosmologie, Université Paris Diderot, CNRS/IN2P3, CEA/lrfu, Observatoire de Paris, Sorbonne Paris Cité, 10, rue Alice Domon et Léonie Duquet, 75205 Paris Cedex 13, France
[2] Aalto University Metsähovi Radio Observatory, Metsähovintie 114, FIN-02540 Kylmälä, Finland
[3] African Institute for Mathematical Sciences, 6-8 Melrose Road, Muizenberg, Cape Town, South Africa
[4] Agenzia Spaziale Italiana Science Data Center, c/o ESRIN, via Galileo Galilei, Frascati, Italy
[5] Agenzia Spaziale Italiana, Viale Liegi 26, Roma, Italy
[6] Astrophysics Group, Cavendish Laboratory, University of Cambridge, J J Thomson Avenue, Cambridge CB3 0HE, U.K.
[7] Astrophysics & Cosmology Research Unit, School of Mathematics, Statistics & Computer Science, University of KwaZulu-Natal, Westville Campus, Private Bag X54001, Durban 4000, South Africa
[8] Atacama Large Millimeter/submillimeter Array, ALMA Santiago Central Offices, Alonso de Cordova 3107, Vitacura, Casilla 763 0355, Santiago, Chile
[9] CITA, University of Toronto, 60 St. George St., Toronto, ON M5S 3H8, Canada
[10] CNRS, IRAP, 9 Av. colonel Roche, BP 44346, F-31028 Toulouse cedex 4, France
[11] California Institute of Technology, Pasadena, California, U.S.A.
[12] Centro de Estudios de Física del Cosmos de Aragón (CEFCA), Plaza San Juan, 1, planta 2, E-44001, Teruel, Spain
[13] Computational Cosmology Center, Lawrence Berkeley National Laboratory, Berkeley, California, U.S.A.
[14] Consejo Superior de Investigaciones Científicas (CSIC), Madrid, Spain
[15] DSM/Irfu/SPP, CEA-Saclay, F-91191 Gif-sur-Yvette Cedex, France
[16] DTU Space, National Space Institute, Technical University of Denmark, Elektrovej 327, DK-2800 Kgs. Lyngby, Denmark
[17] Département de Physique Théorique, Université de Genève, 24, Quai E. Ansermet,1211 Genève 4, Switzerland
[18] Departamento de Física Fundamental, Facultad de Ciencias, Universidad de Salamanca, 37008 Salamanca, Spain
[19] Departamento de Física, Universidad de Oviedo, Avda. Calvo Sotelo s/n, Oviedo, Spain
[20] Department of Astrophysics/IMAPP, Radboud University Nijmegen, P.O. Box 9010, 6500 GL Nijmegen, The Netherlands
[21] Department of Electrical Engineering and Computer Sciences, University of California, Berkeley, California, U.S.A.
[22] Department of Physics & Astronomy, University of British Columbia, 6224 Agricultural Road, Vancouver, British Columbia, Canada
[23] Department of Physics and Astronomy, Dana and David Dornsife College of Letter, Arts and Sciences, University of Southern California, Los Angeles, CA 90089, U.S.A.
[24] Department of Physics and Astronomy, University College London, London WC1E 6BT, U.K.
[25] Department of Physics, Gustaf Hällströmin katu 2a, University of Helsinki, Helsinki, Finland
[26] Department of Physics, Princeton University, Princeton, New Jersey, U.S.A.
[27] Department of Physics, University of California, Santa Barbara, California, U.S.A.
[28] Department of Physics, University of Illinois at Urbana-Champaign, 1110 West Green Street, Urbana, Illinois, U.S.A.
[29] Dipartimento di Fisica e Astronomia G. Galilei, Università degli Studi di Padova, via Marzolo 8, 35131 Padova, Italy
[30] Dipartimento di Fisica e Scienze della Terra, Università di Ferrara, Via Saragat 1, 44122 Ferrara, Italy
[31] Dipartimento di Fisica, Università La Sapienza, P. le A. Moro 2, Roma, Italy
[32] Dipartimento di Fisica, Università degli Studi di Milano, Via Celoria, 16, Milano, Italy
[33] Dipartimento di Fisica, Università degli Studi di Trieste, via A. Valerio 2, Trieste, Italy
[34] Dipartimento di Fisica, Università di Roma Tor Vergata, Via della Ricerca Scientifica, 1, Roma, Italy
[35] Discovery Center, Niels Bohr Institute, Blegdamsvej 17, Copenhagen, Denmark
[36] Dpto. Astrofísica, Universidad de La Laguna (ULL), E-38206 La Laguna, Tenerife, Spain
[37] European Southern Observatory, ESO Vitacura, Alonso de Cordova 3107, Vitacura, Casilla 19001, Santiago, Chile
[38] European Space Agency, ESAC, Planck Science Office, Camino bajo del Castillo, s/n, Urbanización Villafranca del Castillo, Villanueva de la Cañada, Madrid, Spain
[39] European Space Agency, ESTEC, Keplerlaan 1, 2201 AZ Noordwijk, The Netherlands
[40] Helsinki Institute of Physics, Gustaf Hällströmin katu 2, University of Helsinki, Helsinki, Finland
[41] INAF - Osservatorio Astronomico di Padova, Vicolo dell'Osservatorio 5, Padova, Italy
[42] INAF - Osservatorio Astronomico di Roma, via di Frascati 33, Monte Porzio Catone, Italy

[43] INAF - Osservatorio Astronomico di Trieste, Via G.B. Tiepolo 11, Trieste, Italy
[44] INAF/IASF Bologna, Via Gobetti 101, Bologna, Italy
[45] INAF/IASF Milano, Via E. Bassini 15, Milano, Italy
[46] INFN, Sezione di Bologna, Via Irnerio 46, I-40126, Bologna, Italy
[47] INFN, Sezione di Roma 1, Università di Roma Sapienza, Piazzale Aldo Moro 2, 00185, Roma, Italy
[48] IPAG: Institut de Planétologie et d'Astrophysique de Grenoble, Université Joseph Fourier, Grenoble 1 / CNRS-INSU, UMR 5274, Grenoble, F-38041, France
[49] IUCAA, Post Bag 4, Ganeshkhind, Pune University Campus, Pune 411 007, India
[50] Imperial College London, Astrophysics group, Blackett Laboratory, Prince Consort Road, London, SW7 2AZ, U.K.
[51] Infrared Processing and Analysis Center, California Institute of Technology, Pasadena, CA 91125, U.S.A.
[52] Institut Universitaire de France, 103, bd Saint-Michel, 75005, Paris, France
[53] Institut d'Astrophysique Spatiale, CNRS (UMR8617) Université Paris-Sud 11, Bâtiment 121, Orsay, France
[54] Institut d'Astrophysique de Paris, CNRS (UMR7095), 98 bis Boulevard Arago, F-75014, Paris, France
[55] Institute for Space Sciences, Bucharest-Magurale, Romania
[56] Institute of Astronomy and Astrophysics, Academia Sinica, Taipei, Taiwan
[57] Institute of Astronomy, University of Cambridge, Madingley Road, Cambridge CB3 0HA, U.K.
[58] Institute of Theoretical Astrophysics, University of Oslo, Blindern, Oslo, Norway
[59] Instituto de Astrofísica de Canarias, C/Vía Láctea s/n, La Laguna, Tenerife, Spain
[60] Instituto de Física de Cantabria (CSIC-Universidad de Cantabria), Avda. de los Castros s/n, Santander, Spain
[61] Jet Propulsion Laboratory, California Institute of Technology, 4800 Oak Grove Drive, Pasadena, California, U.S.A.
[62] Jodrell Bank Centre for Astrophysics, Alan Turing Building, School of Physics and Astronomy, The University of Manchester, Oxford Road, Manchester, M13 9PL, U.K.
[63] Kavli Institute for Cosmology Cambridge, Madingley Road, Cambridge, CB3 0HA, U.K.
[64] LAL, Université Paris-Sud, CNRS/IN2P3, Orsay, France
[65] LERMA, CNRS, Observatoire de Paris, 61 Avenue de l'Observatoire, Paris, France
[66] Laboratoire AIM, IRFU/Service d'Astrophysique - CEA/DSM - CNRS - Université Paris Diderot, Bât. 709, CEA-Saclay, F-91191 Gif-sur-Yvette Cedex, France
[67] Laboratoire Traitement et Communication de l'Information, CNRS (UMR 5141) and Télécom ParisTech, 46 rue Barrault F-75634 Paris Cedex 13, France
[68] Laboratoire de Physique Subatomique et de Cosmologie, Université Joseph Fourier Grenoble I, CNRS/IN2P3, Institut National Polytechnique de Grenoble, 53 rue des Martyrs, 38026 Grenoble cedex, France
[69] Laboratoire de Physique Théorique, Université Paris-Sud 11 & CNRS, Bâtiment 210, 91405 Orsay, France
[70] Lawrence Berkeley National Laboratory, Berkeley, California, U.S.A.
[71] Max-Planck-Institut für Astrophysik, Karl-Schwarzschild-Str. 1, 85741 Garching, Germany
[72] National University of Ireland, Department of Experimental Physics, Maynooth, Co. Kildare, Ireland
[73] Niels Bohr Institute, Blegdamsvej 17, Copenhagen, Denmark
[74] Observational Cosmology, Mail Stop 367-17, California Institute of Technology, Pasadena, CA, 91125, U.S.A.
[75] Optical Science Laboratory, University College London, Gower Street, London, U.K.
[76] SISSA, Astrophysics Sector, via Bonomea 265, 34136, Trieste, Italy
[77] School of Physics and Astronomy, Cardiff University, Queens Buildings, The Parade, Cardiff, CF24 3AA, U.K.
[78] Space Sciences Laboratory, University of California, Berkeley, California, U.S.A.
[79] Special Astrophysical Observatory, Russian Academy of Sciences, Nizhnij Arkhyz, Zelenchukskiy region, Karachai-Cherkessian Republic, 369167, Russia
[80] UPMC Univ Paris 06, UMR7095, 98 bis Boulevard Arago, F-75014, Paris, France
[81] Université de Toulouse, UPS-OMP, IRAP, F-31028 Toulouse cedex 4, France
[82] Universities Space Research Association, Stratospheric Observatory for Infrared Astronomy, MS 232-11, Moffett Field, CA 94035, U.S.A.
[83] University of Granada, Departamento de Física Teórica y del Cosmos, Facultad de Ciencias, Granada, Spain
[84] Warsaw University Observatory, Aleje Ujazdowskie 4, 00-478 Warszawa, Poland